Energy & Environmental Science

ROYAL SOCIETY OF CHEMISTRY

PAPER

View Article Online
View Journal

Cite this: DOI: 10.1039/d3ee00237c

Morphodynamics of dendrite growth in alumina based all solid-state sodium metal batteries†

Lin Geng,‡[a] Dingchuan Xue,‡[b] Jingming Yao,‡[a] Qiushi Dai,‡[a] Haiming Sun,[ae] Dingding Zhu,[c] Zhaoyu Rong,[a] Ruyue Fang,[b] Xuedong Zhang,[c] Yong Su,[c] Jitong Yan,[ad] Stephen J. Harris,[f] Satoshi Ichikawa,[e] Liqiang Zhang,*[a] Yongfu Tang,*[ad] Sulin Zhang*[b] and Jianyu Huang*[ac]

Received 24th January 2023,
Accepted 27th April 2023

DOI: 10.1039/d3ee00237c

rsc.li/ees

All solid-state batteries (ASSBs) with ceramic electrolytes and alkali metal anodes are a potential future energy storage technology for vehicle electrification and smart grids. However, uncontrollable dendrite growth toward ultimate short circuiting in solid electrolytes (SEs) has become a serious concern in the design of long-cycle, safe ASSBs, and the underlying mechanism has remained unclear. Here through multiscale imaging and morphodynamic tracking we show that Na dendrites grow in β″-Al_2O_3 SEs through an alternating sequence of Na deposition and crack propagation. Atomic-scale imaging evidenced that electrochemical cycling causes massive delamination cracking along the Na^+ conduction planes, accompanied by the closure of neighboring conduction channels. *In situ* SEM observations revealed a dynamic interplay between Na deposition and crack propagation: Na deposition accumulates mechanical stress that induces cracking; cracking releases the local stress, which promotes further Na deposition. Thus, Na deposition and cracking alternatingly proceed until short circuits take place. A multiscale phase-field model is developed to recapitulate the morphodynamics of Na dendrite growth, predicting the tree-like fractal morphology of the growing dendrites. Our findings suggest that decoupling between Na deposition and cracking represents an important route to mitigate uncontrollable dendrite growth in ASSBs.

Broader context

Solid state batteries (SSBs) with higher energy density and better safety are promising than lithium ion batteries. However, it is now understood that dendrites grow even easier in SSBs in some instances, which plagues the performance of SSBs. Understanding the dendrite growth mechanism in SSBs is thus critical to the practical implementation of SSBs. Here we show that dendrite growth in the β″-Al_2O_3 solid electrolyte (SE) exhibits a fractal morphology, and they show a surprising "shape memory effect"; it is suggested that the former is related to the crack propagation, and the latter is attributed to the "dead Na" and the presence of cracks. Atomic scale imaging reveals that deposition/stripping of Na from the SE causes delamination cracks and closure of the conduction planes. These results provide an atomic scale understanding of the chemomechanical failure mechanism of Na SSBs which has important implications for the development of Na SSBs for practical applications.

Introduction

All solid-state batteries (ASSBs) with ceramic electrolytes and alkali metal anodes represent a potential future energy storage technology for vehicle electrification and smart grids.[1–8] However, application of ASSBs is hampered by uncontrollable dendrite growth,[9–11] which causes short circuits, leading to failure and safety issues of ASSBs. Although intensive research

[a] Clean Nano Energy Center, State Key Laboratory of Metastable Materials Science and Technology, Yanshan University, Qinhuangdao 066004, China. E-mail: liqiangzhang85@163.com, tangyongfu@ysu.edu.cn, jyhuang8@hotmail.com
[b] Department of Engineering Science and Mechanics, Pennsylvania State University, University Park, PA 16802, USA. E-mail: suz10@psu.edu
[c] Key Laboratory of Low Dimensional Materials and Application Technology of Ministry of Education, School of Materials Science and Engineering, Xiangtan University, Xiangtan, Hunan 411105, P. R. China
[d] Hebei Key Laboratory of Applied Chemistry, College of Environmental and Chemical Engineering, Yanshan University, Qinhuangdao 066004, P. R. China
[e] Research Center for Ultra-High Voltage Electron Microscopy, Osaka University, Ibaraki, Osaka 567-0047, Japan
[f] Energy Storage Division, Lawrence Berkeley, National Laboratory, Berkeley, CA 94720, USA

† Electronic supplementary information (ESI) available. See DOI: https://doi.org/10.1039/d3ee00237c

‡ These authors contributed equally to this work.

effort has been made to solve the dendrite problem in Li ASSBs,[9,10,12–19] research on dendrite growth in Na ASSBs at room temperature is still in its infancy.[4,20–22] Early studies on Na dendrites in high temperature Na–S batteries were complicated due to high temperature corrosion of the solid electrolytes (SEs, typically β-alumina (β-Al_2O_3) or β″-alumina (β″-Al_2O_3)). Na or S corrosion in room-temperature Na ASSBs may not be as severe as that in high-temperature Na–S batteries; therefore the dendrite growth mechanism may be significantly different. Magnetic resonance imaging (MRI) was used to image Na dendrite growth in β″-Al_2O_3 and revealed a spalling dendritic morphology.[20] Void formation at the Na/β″-Al_2O_3 interface during stripping of Na was previously reported, and accumulation of voids during cycling caused increasing interfacial current density, dendrite formation, short circuits and cell failure.[23] Very recently, it was reported that by using a yttria-stabilized zirconia (YSZ)-enhanced β″-Al_2O_3 SE, the Na/β″-Al_2O_3 interfacial resistance was dramatically reduced, giving rise to a very high critical current density of ~7 mA cm^{-2}.[21] These studies significantly advanced our understanding of the dendrite problem in Na ASSBs. Nevertheless, atomic scale imaging of the dendrite growth in β/β″-Al_2O_3 is highly desired but has not been achieved. Such studies may reveal atomistic mechanisms of the dendrite growth in β/β″-Al_2O_3, thereby offering critical guidance for the development of Na ASSBs.

Here we show that Na dendrite growth in β″-Al_2O_3 proceeds through alternating Na deposition and crack propagation. Our atomic-scale imaging evidenced that electrochemical cycling causes massive delamination cracking along the Na^+ conduction planes, accompanied by the closure of neighboring conduction channels. Scanning electron microscopy (SEM) imaging combined with phase field modeling revealed that Na deposition and crack propagation are intimately coupled and mutually facilitated during dendrite growth. Na deposition elevates local stress to a threshold that drives crack nucleation and propagation, while cracking releases local stress and generates surface conduction channels that speed up subsequent Na deposition. The mechanical and electrochemical processes operate cooperatively in dendrite growth till short circuit occurs. Our understanding of the dendrite morphodynamics suggests that blocking the coupling of the mechanical and electrochemical processes may be an effective route for mitigating uncontrollable dendrite growth in ASSBs.

Results and discussion

In situ optical microscopy (OM) visualization of Na dendrite dynamics in β″-Al_2O_3 SE

We invoke *in situ* optical imaging to track Na dendrite growth dynamics in β″-Al_2O_3 SE. A Na/β″-Al_2O_3/Na symmetric cell was fabricated inside a glovebox under an argon environment. The β″-Al_2O_3 SE was polished to 0.5 mm in thickness, which permitted light transmission for *in situ* OM observations of Na dendrites and crack propagation. Na metal was pressed on the surface of the left and right sides of the β″-Al_2O_3 SE to form a symmetric cell. The two Na electrodes were connected to an

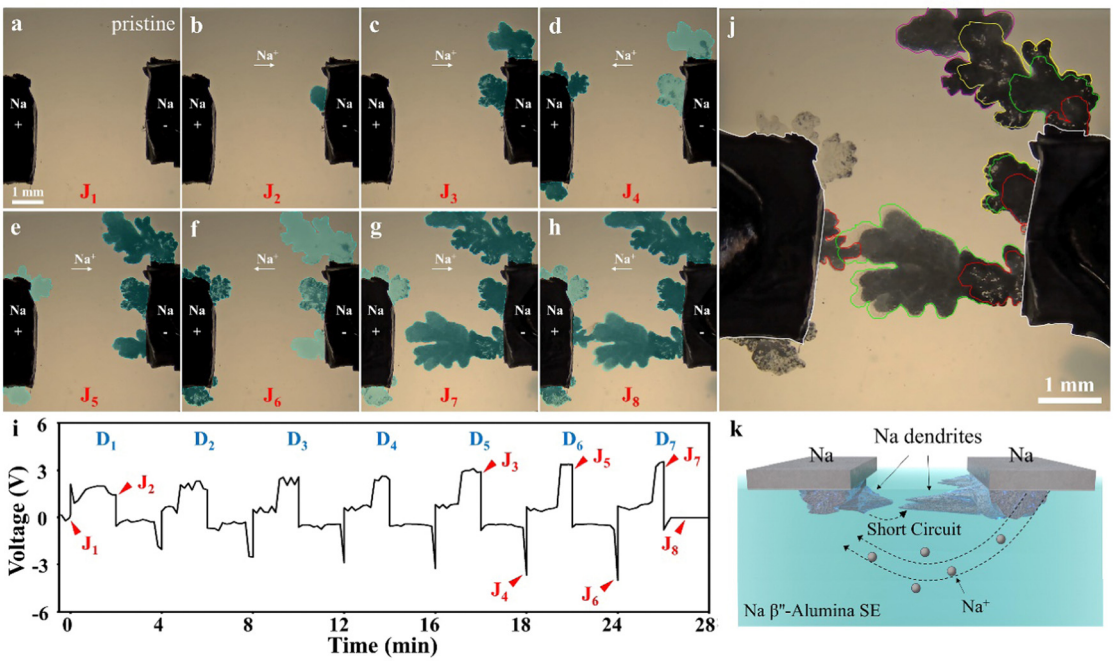

Fig. 1 *In situ* optical microscopy visualization of Na dendrite growth in β″-Al_2O_3 SE in Na/β″-Al_2O_3/Na symmetric cells. (a–h) *In situ* observation of the dynamics of Na dendrite growth. (i) Voltage and current recorded concurrently during *in situ* battery testing corresponding to (a–h). From D_1–D_7 the currents are 0.1, 0.2, 0.4, 0.6, 0.8, 1.0 and 1.2 mA cm^{-2}, respectively. (j) Map of Na metal deposition traces. Red, green, yellow and purple colors outline the deposition traces of the first, second, third and the fourth times, respectively. (k) Schematic illustration of Na dendrite penetration through β″-Al_2O_3 SE. When Na dendrites growing from the two opposite electrodes met in the middle of the SE, short circuit occurred.

electrochemical workstation for galvanostatic charging/discharging experiments (Fig. S1, ESI†), while the corresponding voltage and current were recorded. Fig. 1a–h and Movie S1 (ESI†) show real-time monitoring of Na deposition/stripping within the β″-Al_2O_3 SE at increasing current densities (D_1–D_7, Fig. 1i). At the J_2 point (D_1 = 0.1 mA cm^{-2}, Fig. 1i), a Na dendrite (marked in blue) first nucleated from the middle of the right Na electrode, which then grew toward the left electrode (Fig. 1b). Upon further current flow at a current density of 0.8 mA cm^{-2} (J_3 in Fig. 1i), the Na dendrite propagated further toward the upper-left; in the meantime, a new dendrite emerged from the top of the right electrode, which then propagated toward the upper-left (Fig. 1c). When the current was reversed, the two dendrites on the right electrode were stripped, leaving empty shells behind; concurrently, two new dendrites emerged on the left electrode (Fig. 1d). The deposition and stripping process of Na dendrites continued until short circuit occurred (Fig. 1e–h and k). We have also conducted a series of *in situ* OM experiments under low, medium and high galvanostatic current density to observe Na plating and stripping. Similar dendrite growth phenomena to the gradually increasing current density condition were observed under the constant current mode of plating/stripping (Fig. S2, ESI†).

Interestingly, the deposition/stripping of Na dendrites always followed the same paths as in previous cycles (Fig. 1j), exhibiting a ''memory'' phenomenon. The memory effect may arise from the following reasons: first, due to the presence of residual Na metal the old path may have a stronger electrical field that attracted Na^+; second, dendrite growth and propagation in the early cycles may have generated cracks and voids in the SE, which became the preferred Na deposition/stripping paths because of the reduced Na deposition barrier. This path-dependent cell polarization arises from the chemomechanical coupling effect during Na deposition.[14,24] According to the Butler–Volmer equation, the Na deposition rate depends on the kinetic barrier: $i \sim \exp(F\Delta\phi - \sigma_m\Omega_{Na})$, where F is Faraday's constant, Ω_{Na} is the molar volume of Na (24 cm^3 mol^{-1}), σ_m is the local compressive stress, and $\Delta\phi$ is the overpotential. The generated cracks and voids along the old path reduce the compressive stress, thereby decreasing the kinetic barrier for Na deposition and increasing the deposition rate.

In the voltage *versus* time profile (Fig. 1i and Fig. S3, ESI†), we found two types fluctuation during plating and stripping: one involved large voltage jump, and the other consisted of small ripples. During plating, the emergence of new Na deposition sites was always accompanied by a voltage jump to higher polarization (Fig. S3j, I → J, P → Q, ESI†), whereas relatively low polarization occurred when Na deposited along the previous paths. During stripping, a large voltage jump was also observed (Fig. S3j, F → G, M → N, ESI†), which was caused by the following reason: under a constant current mode, the deposited Na on the right electrode was not sufficient to replenish the deposition on the left electrode due to the existence of ''dead'' Na on the right electrode; therefore, stripping of ''fresh'' Na from the right electrode was needed, which may require new activation, and result in high overpotential. The ripples observed during plating/stripping are possibly due to the change in the ion diffusion distance.[13] For example, during deposition, as the deposition front advances, the ion travel distance changes accordingly (Fig. S3k and l, ESI†).

To characterize the morphology of Na dendrites inside the electrolyte, the β″-Al_2O_3 electrolyte pellet was mechanically sliced to expose the cross-section of the SE (Fig. 2a and b). Immediately after slicing, one half of the specimen was transferred into a scanning electron microscope using a home-made sample transfer kit that protected the samples from air exposure. The SEM image of the sliced surface is presented in Fig. 2c (Na shadowed in blue), and an enlarged view of a designated area labelled ''1'' is shown in Fig. 2e. Multiple Na-filled cracks were observed (Fig. 2d, e and Fig. S4, ESI†). A magnified view of area ''2'' in Fig. 2c shows an interesting web-like structure (Fig. 2f). Elemental mapping (Fig. 2g–j) of Na, Al and O confirmed that the web-like structure is composed of Na metal. Fig. S5 (ESI†) shows the elemental mapping of the Na dendrites and β″-Al_2O_3 interface. The disparate distribution patterns of Na and O suggest that the web-like structure is Na metal without oxidation. Moreover, transgranular fracture occurred for β″-Al_2O_3 (Fig. S6, ESI†) and the fracture surfaces were filled with web-like Na metal, indicating an interplay between Na deposition and cracking. Web-like dendrite structures were also observed on the surface of polycrystalline β″-Al_2O_3 (Fig. S7, ESI†), which were similar to the web-like dendrite structures in $Li_7La_3Zr_2O_{12}$ (LLZO),[12] suggesting great similarity in the dendrite growth mechanism between Li and Na. Remarkably, a magnified view of the dendrite web indicates that some of the dendrites resided on the transgranular surface of a single crystal β″-Al_2O_3 grain (Fig. 2f and Fig. S8, ESI†), which is in distinct contrast to the Li web structures predominantly formed along the grain boundaries of LLZO SE.[12] We have compared the average size of the web unit structure between single and polycrystal samples. The analysis showed a size distribution from 0.6 to 4.2 μm with a mean size of 1.86 ± 0.77 μm for single crystal samples (Fig. S9a, ESI†), and from 1 to 8 μm with the mean size of 3.86 ± 1.32 μm for polycrystal samples (Fig. S9b, ESI†).

High-angle annular dark-field (HAADF) image characterization of short circuited β″-Al_2O_3 SE

To elucidate the Na dendrite growth mechanism in β″-Al_2O_3 SE on an atomic scale, HAADF imaging of the β″-Al_2O_3 samples after short circuit was conducted (Fig. 3). β″-Al_2O_3 is composed of alternating closely-packed spinel slabs and loosely-packed Na–O layers (Fig. 3a–c). The loosely-packed layers are the Na^+ conduction planes along which Na^+ is free to move under an electric field. The closely-packed oxide slabs comprise four layers of O ions with Al ions in both octahedral (marked in blue in Fig. 3c) and tetrahedral (marked in pink in Fig. 3c) coordinates. The adjacent spinel blocks are connected by an oxygen ion with surrounding mobile Na^+ to form the conduction planes (Fig. 3c). We noted that some of the conduction planes were closed due to the *c*-axial shift of two neighboring spinel blocks after cycling (Fig. 3d–f). The shift of the spinel

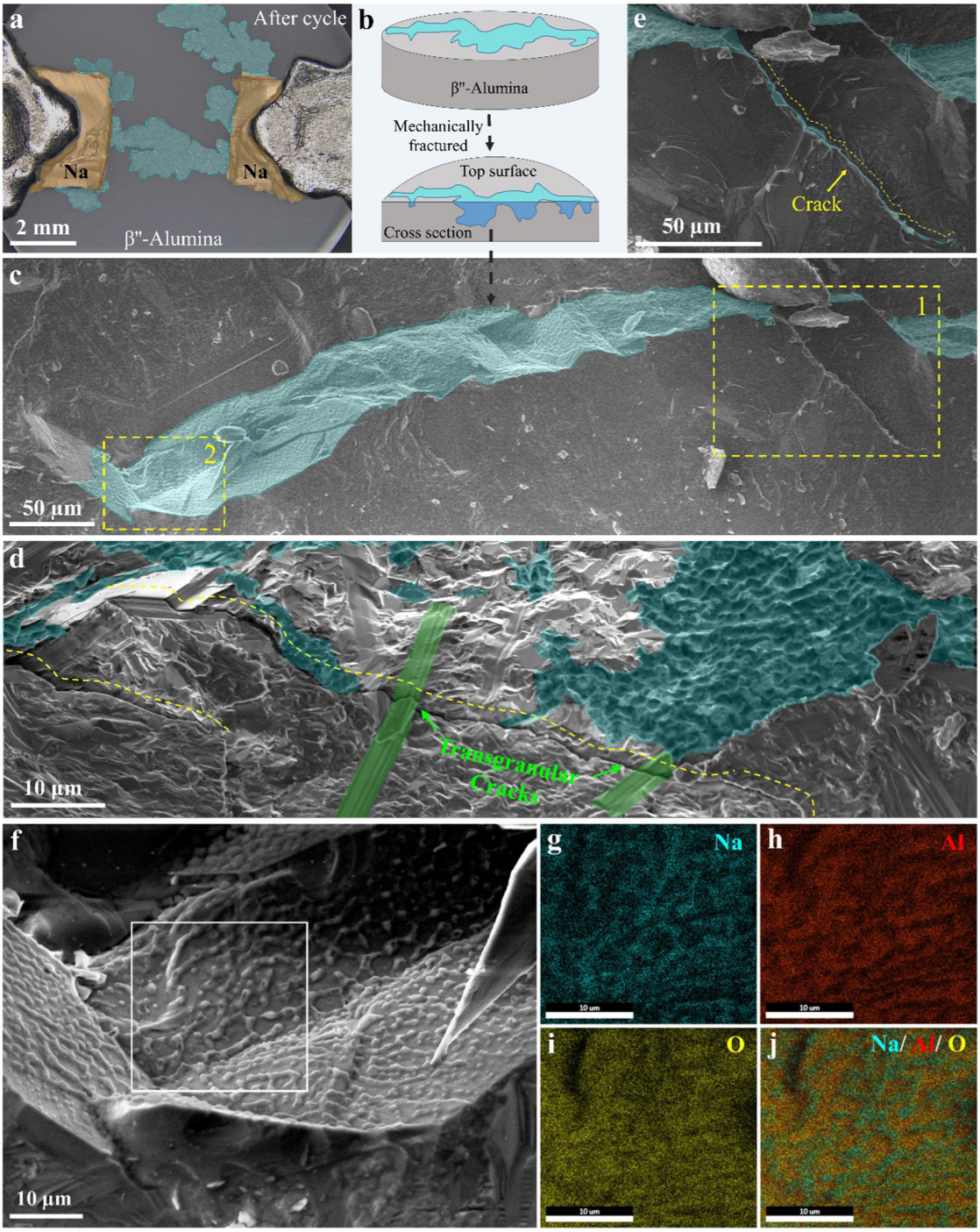

Fig. 2 SEM characterization of the β''-Al_2O_3 SE after cycling. (a) An optical image of the Na/β''-Al_2O_3/Na symmetric cell after cycling, showing large-scale Na dendrite (light blue) short circuiting. (b) Schematic illustration of a cross-sectional view of the Na dendrites and cracks. The cross-section was obtained by mechanically cutting of the short-circuited SE pellet. (c and d) SEM images showing cross-sectional view of the Na dendrites and cracks. The blue-shaded area is the cracked surface, in which many web-like Na dendrites were deposited. (e) SEM images of Na-filled cracks corresponding to the boxed region "1" in (c). (f) Magnified view of the web-structured Na dendrites corresponding to the boxed region "2" in (c). (g–j) Elemental mapping images of the web-like structured Na in β''-Al_2O_3 SE corresponding to the boxed regions in (f).

blocks was accompanied by the gliding of the spinel block along the [−110] direction (route "1" in Fig. S10, ESI†) or the [210] direction (route "2" in Fig. S10, ESI†), producing stacking-faults between two neighboring spinel blocks where the conduction planes were closed. As a result, the corner-sharing AlO_4 tetrahedra became edge-sharing AlO_4 tetrahedra to maintain the structural stability (Fig. 3e, f). Simply, O_1, O_2, O_3 atoms marked in orange in Fig. 3c follow the path shown by the black arrow to reach the position O_4, O_5, and O_6 (marked in green), respectively. All the HAADF images match well with the

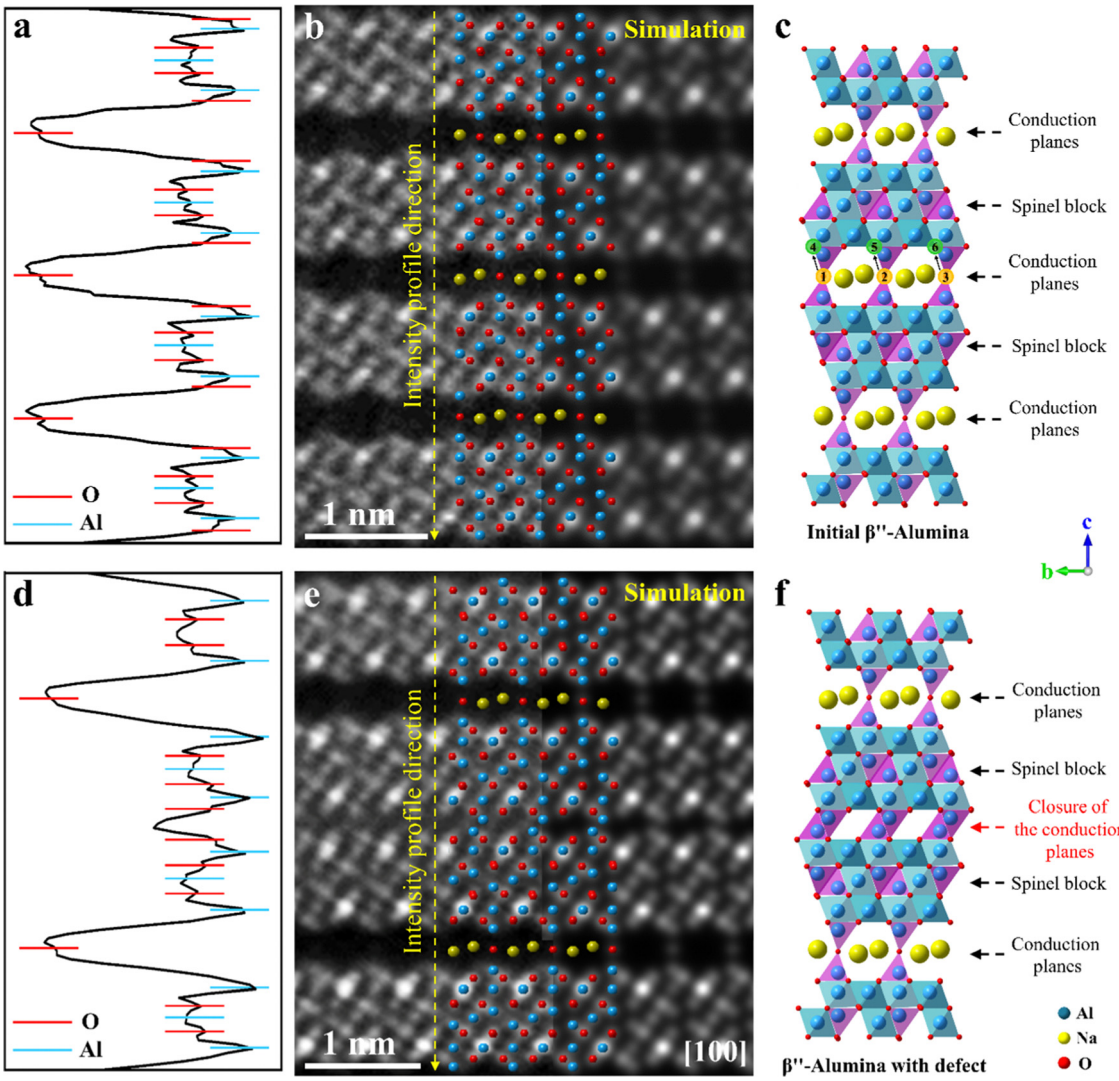

Fig. 3 Atomic structures of β″-Al_2O_3 SE with/without conduction plane closure. (a) Intensity profile along the yellow dashed line of initial, intact β″-Al_2O_3. (b) HAADF image of the initial β″-Al_2O_3 structure. (c) Atomic structure model of the initial β″-Al_2O_3 structure. (d) Intensity profile along the yellow dashed line in β″-Al_2O_3 SE with conduction plane closure caused by electrochemical cycling. (e) HAADF image of the closure of the conduction planes in β″-Al_2O_3 SE. (f) Atomic structure model of conduction channel closure in β″-Al_2O_3.

simulated HAADF images (Fig. 3 and Fig. S11, ESI†). We further noted that electron beam irradiation can also cause the conduction plane closure (Fig. S12, ESI†). The conduction plane closure is ascribed to Na^+ depletion induced instability of the conduction planes. To clarify whether the closure of the conduction planes was caused electrochemically or pre-existed in the as-sintered samples, we recorded HAADF images of the ceramic electrolyte before and after cycling as shown in Fig. S13 (ESI†). In the pristine as-sintered samples, no Na^+ conduction planes closure was found (Fig. S13a–f, ESI†). In contrast, the grains after electrochemical cycling show many regions of "closure of the conduction planes" (Fig. S13g–i, ESI†).

Low magnification HAADF images (Fig. 4a) shows multiple delamination cracks with kinks (outlined by yellow dashed lines) in the β″-Al_2O_3 grain. Atomic scale HAADF images indicate that the cracks propagated along Na^+ conduction planes (Fig. 4b). A kink along the conduction planes (Fig. 4c) and fracture of the spinel blocks perpendicular to the conduction planes (Fig. 4d) were also detected in the middle of the crack. Delamination cracks were also found in other β″-Al_2O_3 grains after cycling of a Na/β″-Al_2O_3/Na cell (Fig. S14 and S15, ESI†), demonstrating the generality of this phenomenon. The SEM image of β″-Al_2O_3 SE after *in situ* OM cycling shows that most of the delamination cracks are filled with Na (Fig. S16, ESI†). Fracture in single crystalline β″-Al_2O_3 occurs predominantly along the conduction planes that are parallel in space, which indicates a parallel stripe-like structure of the Na dendrites. However, since crack kinking also occurs, we suspect that cracking kinking makes the cracks interconnected and fractal, which supports the web-like structure of Na dendrites in single crystalline β″-Al_2O_3 SEs. Low magnification HAADF images show that the cracks can be both transgranular (Fig. S17, ESI†) and intergranular (Fig. S18, ESI†). The simultaneous occurrence of the closure of Na^+ conduction planes, Na dendrite growth, and

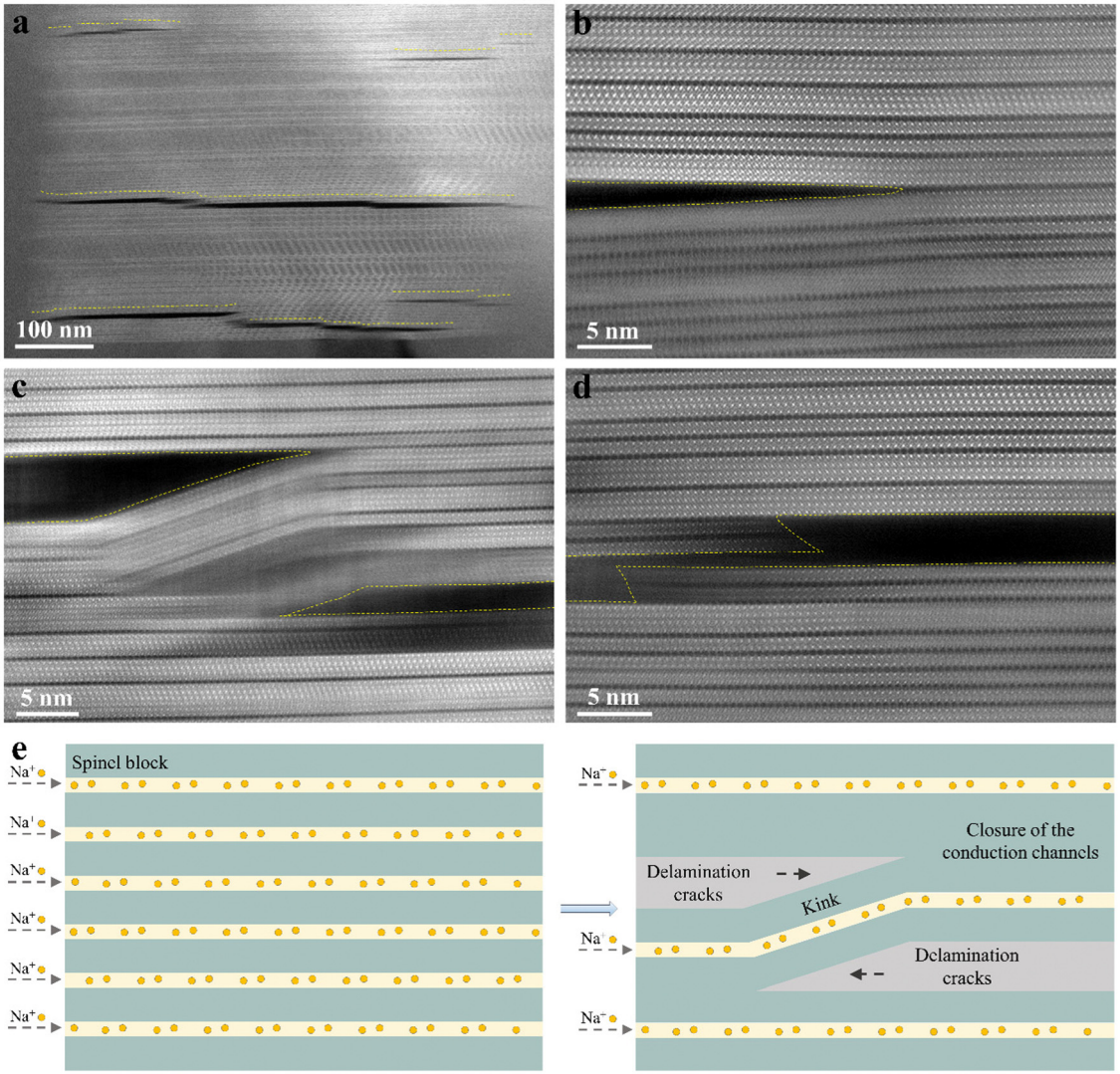

Fig. 4 HAADF characterization of delamination cracks in β″-Al_2O_3 SE after electrochemical cycling. (a) Low magnification HAADF image of delamination cracks (outlined by yellow dashed lines) distributed in a β″-Al_2O_3 grain. (b) Atomic scale imaging of the delamination crack tip. (c) A kink along the conduction planes. (d) Fracture of the spinel blocks along the vertical direction to the conduction planes. (e) Schematic illustration of the formation of the delamination cracks.

crack propagation suggest that these events are closely correlated and interdependent (Fig. 4e). Moreover, HAADF imaging of the β″-Al_2O_3 samples after short circuit in a Na/β″-Al_2O_3/Na actual symmetric battery operated at 80 °C shows closure of the conduction planes and delamination cracks along the Na^+ conduction planes (Fig. S19, ESI†), which is consistent with the *in situ* OM results, demonstrating the generality of this phenomenon in alumina based all solid-state sodium metal batteries.

In situ SEM visualization of Na dendrite growth and crack propagation in β″-Al_2O_3 SE

To investigate the growth dynamics of metallic Na dendrites on a mesoscale, a Na ASSB micro-battery was constructed in a focused ion beam-scanning electron microscopy (FIB-SEM) system, which enabled operando monitoring of the structural evolution of the micro-battery during operation. A β″-Al_2O_3 ceramic pellet with a diameter of 12 mm and a thickness of 1 mm was broken into several small pieces, and one piece was pressed into a Na metal electrode and assembled on an SEM sample stub, which was further connected to one terminal of an external power supply (Fig. 5a). A square-shaped micro-Pt electrode with a size of 10 μm × 10 μm was deposited *via* Ga^+ ion beam sputtering on the top surface of the β″-Al_2O_3 SE and used as a counter electrode. A W tip was positioned to make contact with the Pt electrode, and the other end of the W tip was connected to the second terminal of the potentiostat. For a better visualization of the dendrite and crack dynamics, the β″-Al_2O_3 SE was positioned in such a configuration that both the top and side surfaces were visible (Fig. 5b).

Upon applying a negative potential to the Pt electrode, Na metal (marked in blue) emerged first from the top and then from the side (Fig. 5c). At 186 s, a crack (outlined by a yellow dotted line) appeared on the side surface of the β″-Al_2O_3 SE and Na metal extruded out at the lower-right segment of the crack

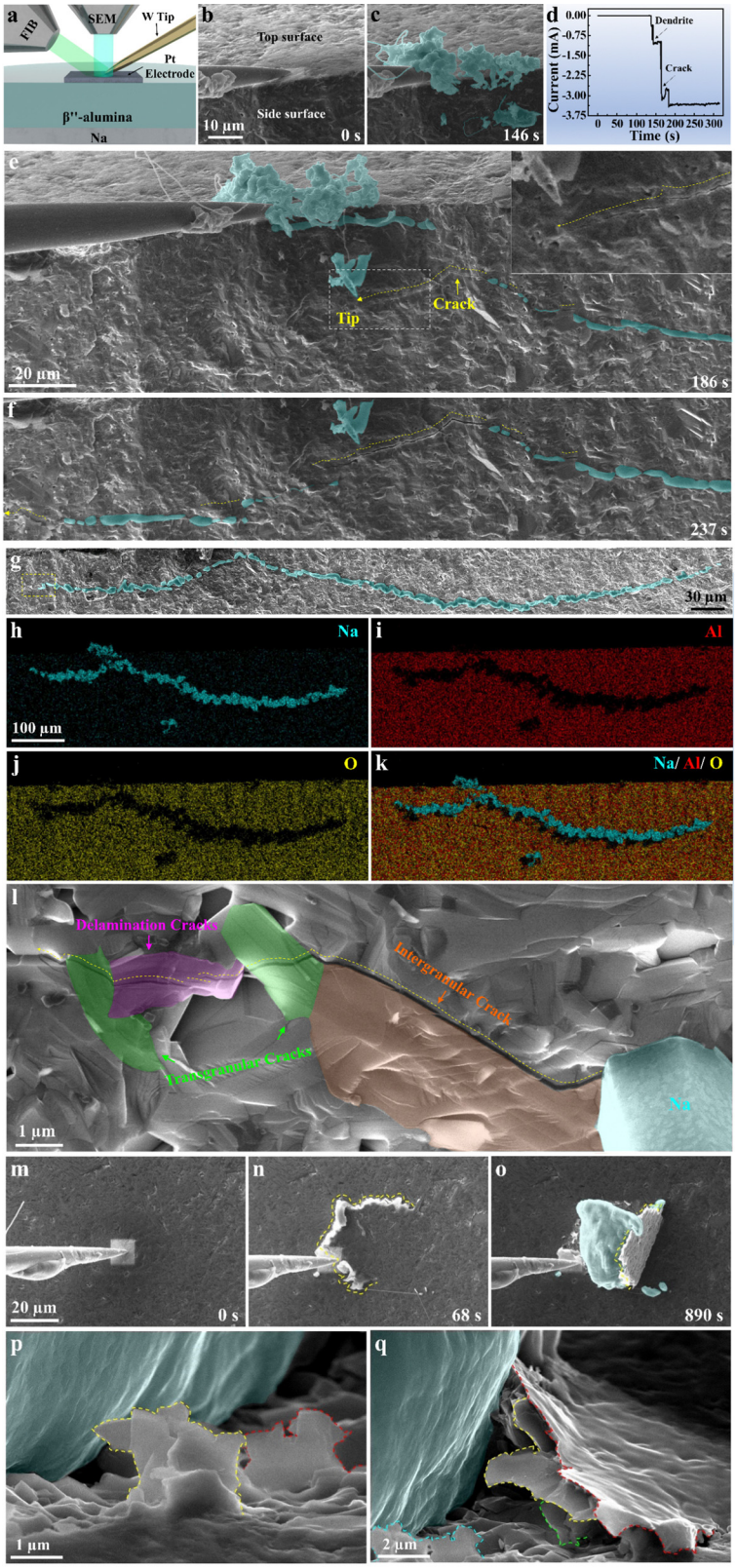

Fig. 5 *In situ* SEM observations of Na deposition and cracking in the SE in a mesoscale FIB-SEM-based ASSB. (a) Schematic illustration of the *in situ* micro-battery testing setup. A Pt electrode was deposited on the top surface of the β″-Al_2O_3 SE for Na deposition. Na metal was used as a counter electrode. (b and c) SEM images showing Na metal deposition on the top surface and cross-section of the β″-Al_2O_3 SE. (d) Current *vs.* time plots corresponding to Na deposition and crack propagation. (e and f) A cross-sectional view of the formation of a bowl-shaped crack and Na filling the crack. The yellow dashed lines outline the cracks on the cross-section and blue-shaded area marks Na dendrites. (g) A full view of the bowl-shaped crack on the cross section of the SE. (h–k) Elemental mapping images of the Na filled crack in β″-Al_2O_3 SE. (l) High magnification view of the crack tip corresponding to the boxed region in (g), showing transgranular, intergranular and delamination cracks, which are marked in green, orange and pink, respectively. (m–o) *In situ* observation of the dynamic process of a sheet-like β″-Al_2O_3 SE pushed up by deposited Na metal. (p and q) Magnified view of thin sheets peeled off during Na dendrites growth.

(Fig. 5e, top right illustration shows a magnified view of the crack tip boxed in white dotted lines). Upon further Na deposition, the crack widened and the crack tip (marked by a yellow arrow) continued to propagate toward the lower-left (Fig. 5f). In the meantime, more Na extruded out of the existing crack. It appeared that Na deposition always trailed the crack propagation until all the cracks were filled with metallic Na (Fig. 5g), consistent with visualizations by Bruce *et al.* and Huang *et al.*[15,25] In fact, neither metallic Na nor Li conformally followed up with the crack tip as no metal was detected at the crack tip. Thus, crack propagation in these cases is not driven by direct metal pushing at the crack tip, but possibly by the opening force at the tail of the crack due to the deposited Na metal. Similar Na deposition and crack propagation dynamics in β″-Al_2O_3 SE was observed in other experiments (Fig. S20, ESI†), suggesting the robustness of the mechanism. Concurrent current recording indicated that the Na metal deposition and cracking were correlated to two consecutive sudden current jumps (Fig. 5d), implying that both Na deposition and cracking induced a large electronic conductivity increase of the β″-Al_2O_3 SE, leading to a micro-short circuit. With further Na deposition and crack propagation, the short circuit became aggravated. SEM images with the corresponding elemental mapping of the side surface of β″-Al_2O_3 SE (Fig. 5g–k) revealed that two "bowl-shaped" cracks with lengths of 150 and 420 μm formed under the surface of the β″-Al_2O_3 SE, similar to Li dendrite induced crack patterns in LLZO SE.[15] Another top view *in situ* experiment confirmed the formation of "bowl-shaped" cracks (Fig. S21, ESI†). Similar "bowl-shaped" cracks were also found in β″-Al_2O_3 SE after *in-situ* optical cycles (Fig. S22, ESI†), demonstrating the generality of this phenomenon in β″-Al_2O_3 ASSBs. More detailed inspection revealed both transgranular (shaded in green) and intergranular (shaded in orange) cracks (Fig. 5l). Interestingly, transgranular cracks, previously referred to delamination cracks, were predominantly found along Na^+ conduction planes in the interior of β″-Al_2O_3 grains (shaded in pink in Fig. 5l). The *in situ* SEM experimental results corroborate well with HAADF image characterization of short circuited β″-Al_2O_3 SE after electrochemical testing (Fig. 4 and Fig. S14, S15, S17, S18, ESI†).

The generation of delamination cracks by Na deposition along the Na^+ conduction planes was observed directly by *in situ* SEM. The W tip was positioned to make contact with the Pt electrode deposited on the top surface of β″-Al_2O_3 SE (Fig. 5m). As a negative potential was applied to the Pt electrode, a semicircular crack with sharp contours appeared on the top surface of the β″-Al_2O_3 disk (Fig. 5n). Na dendrites emerged as soon as the crack appeared. As more Na was extruded, a slice of SE was peeled off and lifted up the SE matrix (Fig. 5o). Many sheet-like structures (outlined by yellow, red, green and blue dashed lines, respectively, Fig. 5p and q) were found in the β″-Al_2O_3 SE matrix where the surface SE was peeled off. Apparently, the SE sheet debris was peeled off from the layered β″-Al_2O_3 grain along the Na^+ conduction planes, which is similar to the peeling of a graphene layer from highly orientated pyrolytic graphite. The structure of β″-Al_2O_3 consists of spinel blocks stacked along the *c*-axis, and the interlayer binding force is presumably weak due to a large lattice spacing (6.35 Å) between two neighboring blocks. Therefore, these spinel blocks are easily delaminated under tensile stress generated by Na dendrite growth. The weak interlayer binding is further manifested in the following experiment in which the W tip was connected to the edge of the Na^+ conduction planes on the single crystal grain (Fig. S23, ESI†). Once a negative potential was applied, Na dendrites deposited along the Na^+ conducting layer (Fig. S23b, ESI†). With further Na deposition, cracks appeared. Meanwhile, a flake of β″-Al_2O_3 layer (outlined by yellow dashed lines, Fig. S23c, ESI†) was lifted off by Na metal growth. Na deposition along the delamination cracks was clearly observed in the magnified SEM image (Fig. S23d, ESI†). The SEM images with the corresponding elemental mapping show a flake of β″-Al_2O_3 surrounded by Na metal, confirming the existence of delamination cracks along the Na^+ conduction planes (Fig. S23d–h, ESI†). These *in situ* SEM observations (Fig. 5 and Fig. S23–S25, ESI†) thus confirm the growth of delamination cracks. Apparently, these delamination cracks served as the initial crack configurations for further Na dendrite growth and cracking in β″-Al_2O_3 SE.[26]

A multiscale view of conduction plane closure, crack propagation, and Na dendrite growth

The multiscale imaging supports the Na dendrite growth mechanism that involves a close interplay between Na deposition and crack propagation. During electrochemical cycling, uneven Na^+ flow and temporary depletion of Na^+ may cause the closure of some conduction planes and separation of others, generating delamination microcracks. These delamination cracks are conduction highways of Na^+ and likely the nucleation sites for Na deposition. Deposited Na metal further increases Na^+ conductivity along the highways, promoting Na deposition and Na dendrite growth. However, continuous Na deposition generates volumetric strain and stress at the tip of the growing Na dendrite, slowing down Na deposition. When the deposition stress reaches a threshold, crack propagates, releasing the stress and creating a highly conductive channel for Na^+ transport. These two essential processes, *i.e.*, Na deposition and cracking, proceed alternatively until a short circuit occurs.

To further appreciate the Na dendrite morphological evolution and growth mechanism in β″-Al_2O_3 SEs, we developed a multiscale, multi-phase field model to simulate the coupled mechanical and electrochemical process. In the model, we followed the dynamics of five independent phase fields in space $\boldsymbol{x}$ and time t: the displacement field $\boldsymbol{u}(\boldsymbol{x}, t)$ that simulate stress generation and release in the SE, the electrical potential $\eta(\boldsymbol{x}, t)$ that drives Na^+ diffusion, the Na^+ concentration field $c(\boldsymbol{x}, t)$ that simulates Na^+ diffusion, the Na metal phase $\xi(\boldsymbol{x}, t)$ that simulates Na deposition, and the fracture phase $d(\boldsymbol{x}, t)$ that simulates crack nucleation and propagation. Within the phase-field framework, we constructed a free energy functional in terms of the phase fields for the system, from which the corresponding kinetics equations can be followed (ESI†). Solving the kinetics equations and mechanics equilibrium equation simultaneously allow us to obtain information on

the stress distribution, electrical potential, crack extension, and dendrite growth.

We first applied our model at the microscopic level, as shown in Fig. 6a, to simulate delamination crack inside individual grains. Nucleation of Na dendrites likely occurs along the conduction channel at the SE/metal interface. Once nucleated, further Na deposition along the conduction channels is kinetically favorable due to the locally increased electrical field that attracts Na^+ toward the dendrite front. Na deposition generates volumetric strain and stress locally at the deposition site. The maximum compressive stress can reach $\sigma_{m,max} = F\Delta\phi/\Omega_{Na}$. For an applied overpotential of 2.2 V, the maximum compressive stress can reach as high as 8.8 GPa, which is an idealized estimation under the assumption that the voltage drop $\Delta\phi$ exclusively occurs at the charge-transfer interface (the deposition site). When the deposition stress reaches the fracture stress of the grains, crack nucleates and propagates along the conduction channel (Fig. 6b). Thus, the deposited Na metal acts as a wedge for cracking. The wedge crack is stable and rests after propagating for a certain distance. Our simulations show that the crack tip always runs ahead of the dendrite tip, consistent with the experimental observations. Crack propagation releases the local stress, which speeds up further Na deposition according to the Butler–Volmer kinetics. The fracture surfaces act as a superior conduction channel for Na^+ diffusion, which further accelerates Na deposition and dendrite growth therein. Thus, Na deposition and crack propagation are two mutually reinforcing processes that alternatingly occur during dendrite growth. Once the crack runs through an entire grain, it may reach a triple junction of three grains. The crack may bifurcate into two directions owing to the anisotropic fracture strengths and directional conduction channels, causing fractal fracture (Fig. 6b). Noteworthy, the fracture strength of the solid electrolyte (β''-Al_2O_3) is typically about 300 MPa,[21,26] considering inevitable flaws. Within each grain, the conduction planes are weak and prone to cleavage fracture. We set the fracture strength along the conduction planes one order of magnitude lower than that in other directions. In our experiments, we observed both intra- and intergranular fracture, which suggests that the fracture strength of the grain boundaries is comparable to that of the conduction planes of the grains.

To simulate the specimen-scale morphodynamics of the Na dendrite growth shown in Fig. 1, the microscopic model considering individual grains is computationally prohibitive. Here we extended the microscopic phase field model to a macroscopic scale by information passing across different length scales. In the macroscopic model, the fracture phase is not explicitly simulated, but represented by a damaged domain that causes local stress release and increased Na^+ diffusion kinetics. When the local stress due to Na deposition reaches the threshold σ_{m_0}, a damaged domain encompassing the region of highly localized tensile stress can be identified. Assigning a vanishing modulus and increased Na^+ diffusivity to the damaged domain mimics the generation of the fracture phase. The directional path of further Na deposition is assumed to be random within the damaged domain, in accordance with the random orientation of the grains in the SE. Following this simplified model, our simulation in Fig. 6c predicts the tree-like fractal morphology of Na dendrites,

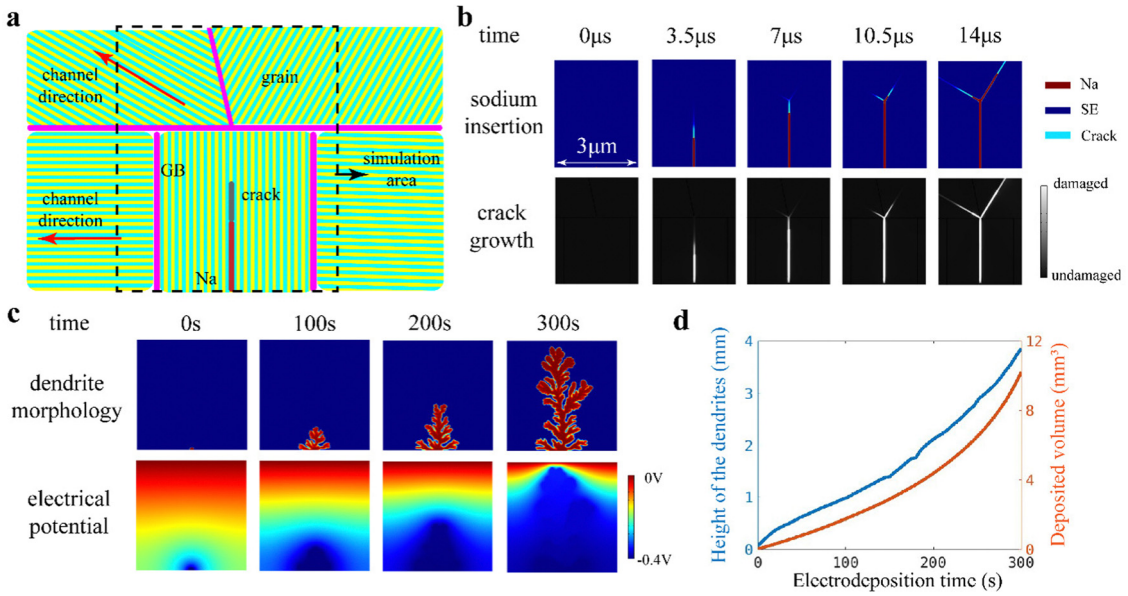

Fig. 6 Multiscale multi-phase field modeling of Na dendrite growth and crack propagation in the β''-Al_2O_3 SEs. (a) Schematic illustration of the interplay between the Na dendrite growth and crack extension within polycrystal grains. Each grain orients differently, giving rise to different conduction channel directions. The fracture toughness of grains is also orientation dependent. (b) Modeling results show Na deposition can cause crack propagation within the β''-Al_2O_3 grain. The crack tip always runs ahead of the dendrite front. Both the crack and dendrite alter their growth direction at the triple junction at which multiple grains meet. (c) Simulated morphological evolution of the growing Na dendrite. The dendrite morphology appears due to the fractal cracking in the SEs. (d) Growth kinetics of the dendrite by plotting the height and volume as a function of cycling time. The dendrites grew progressively faster both in height and volume. The averaged current density is 1 mA cm^{-2} and the thickness of the dendrite is assumed as 3 μm.

which agrees astonishingly well with the experimental observations shown in Fig. 1. Fig. 6d plots the simulated growth kinetics of Na dendrites in terms of the height and overall volume of the dendrites. Despite of constant average current density, the deposition rate gradually increases as the dendrite propagates toward the stripped electrode. When the dendrite front is far away from the stripped electrode, dendrite growth is limited by Na^+ diffusion and relatively slow. As the dendrites get closer to the stripped electrode, the diffusion path becomes shorter, and the Na^+ concentration becomes higher at the dendrite front, leading to the increased deposition rate. However, the growth rate of the dendrite height increases less markedly owing to its fractal expansion. The simulated morphological evolution and dendrite growth kinetics may be applicable to other ceramic electrolytes.

Conclusions

In summary, *in situ* imaging of the dynamics of Na deposition and crack propagation in β″-Al_2O_3 SE were conducted *via* OM and SEM systems. The mechanisms leading to Na β″-Al_2O_3 SE failure were revealed by atomic scale HAADF imaging. Our major conclusions are as follows.

1. Na dendrite growth exhibits "memory" effects, *i.e.*, new growth always follows the old paths.

2. We have provided direct evidence that web Na existing on the surface of single crystal grains can propagate transgranularly through β″-Al_2O_3 grains, resulting in short-circuiting of the Na/β″-Al_2O_3/Na symmetric cells during cycling.

3. HAADF imaging reveals that Na^+ conduction causes the closure of conduction channels of β″-Al_2O_3; high current density triggers massive delamination cracks along the conduction planes and the fracture of the spinel blocks along the direction perpendicular to the conduction planes.

4. *In situ* SEM observations revealed the dynamics of the interplay between Na deposition and crack propagation: namely, Na deposition-induced cracks run ahead of Na deposition; Na deposition triggers new cracks; and Na deposition trails crack until short circuit occurs.

This study provides a multi-length-scale investigation of Na dendrite deposition and crack propagation, which enhances the understanding of the failure mechanism of β″-Al_2O_3 SE in Na ASSBs, thus providing critical science to guide the development of Na ASSBs for energy storage applications.

Experimental section

In situ OM electrochemical setup

The β″-Al_2O_3 ceramic disks were purchased from Jining CreaTech New Energy Technology Co., Ltd. The pellet had a diameter of 12 mm, a thickness of 0.5 mm, and a density of 99.6%. In the battery setup, Na metal (3 mm × 2 mm × 0.2 mm) was pressed on the two ends of the surface of the β″-Al_2O_3 ceramic disk, which was finely polished to a thickness of 0.5 mm to remove Na_2CO_3 contamination and make the solid electrolyte slight transparent. The assembled Na/β″-Al_2O_3/Na symmetric cell was heated to 250 °C for 10 minutes on a heating station placed in an argon protected glovebox to improve the contact between Na and SE. After cooling to room temperature, the two Na electrodes were connected to an electrochemical workstation (LAND CT 3001A) for galvanostatic charge/discharge experiments, while the corresponding voltage and current were recorded concurrently. The experiment was conducted in an argon environment inside a glovebox (O_2 < 1 ppm, H_2O <1 ppm).

In situ SEM electrochemical platform

The experiment was conducted in an FIB-SEM system (Helios G4 CX, Thermo Fisher Scientific). In a micro-battery setup, a W tip was connected to a Pt electrode deposited on top of the β″-Al_2O_3 surface, and this W tip was also connected to the negative terminal of a potentiostat (2612B Source Meter, Keithley). A β″-Al_2O_3 ceramic disk with a diameter of 12 mm and a thickness of 1 mm was broken into small pieces, and one piece of about 5 mm was pressed onto a Na metal, which was attached to an SEM sample stub that was connected to the other terminal of the potentiostat.

On the top surface of the β″-Al_2O_3 disk, a Pt electrode pad was deposited using ion beam-induced deposition at 30 kV, 80 pA. A W tip (also called "easy-lift") was positioned to make contact with the Pt electrode. To investigate the delamination crack nucleation and propagation during Na deposition, the W tip was also connected to the conduction planes of a single crystalline grain of β″-Al_2O_3. This was feasible because β″-Al_2O_3 has a layered structure with conduction planes visible under SEM.

HAADF characterization

HAADF samples were prepared using a dual-beam FIB system (Helios G4 CX, Thermo Fisher Scientific) operating at 2–30 kV. A protective thin Pt layer was deposited over the region of interest before milling. A standard lift-out procedure was used to directly prepare thin slices from β″-Al_2O_3 SE after the cycling of micro-batteries; then the slices were glued to a half Cu grid and milled to 7 μm × 3 μm × 100 nm rectangular sheets.

HAADF images were acquired on a Cs-corrected scanning transmission electron microscope (STEM, Titan cubed Themis Z 300 kV, Thermo Fisher Scientific), which was equipped with a DCOR spherical aberration corrector for the electron probe, and a quad-silicon drift detector (Super-X) optimized for rapid X-ray collection. To avoid specimen damage and obtain reliable images, the beam current was adjusted to be as low as possible. Typically, a beam current of 12 pA was applied; according to STEM dosimetry,[27] the dose per frame is: $D_f = (I_b/A)\, t_a$, where I_b is the beam current (12 pA), t_a is the acquisition time (20.0 s) and A (2.68×10^5 Å^2) is the frame area on the sample; thus we got a value of D_f = 5600 e Å^{-2}. The HAADF image simulations were performed using an xHREM program, which was based on the multislice method.[28]

Author contributions

J. Y. H., Y. F. T. and L. Q. Z. conceived and designed the project. L. G., D. D. Z. and M. J. Y. prepared the sample. L. G., J. M. Y.

and Z. Y. R. carried out *in situ* SEM experiments. Q. S. D. carried out *in situ* OM experiments. L. G. carried out HAADF characterization. D. C. X., R. Y. F. and H. M. S. performed computational modelling. L. G., X. D. Z, Y. S. and J. T. Y. contributed to data analysis. J. Y. H., Y. F. T., S. L. Z and L. G. wrote the paper. All the authors discussed the results and commented on the manuscript.

Conflicts of interest

The authors declare no conflict of interest.

Acknowledgements

This work was financially supported by the National Natural Science Foundation of China (no. 52022088, 51971245, 51772262, 21406191, U20A20336, 21935009, and 22279112), the Fok Ying-Tong Education Foundation of China (no. 171064), the Beijing Natural Science Foundation (2202046), the Natural Science Foundation of Hebei Province (no. F2021203097, B2020203037, B2018203297, and B2022203018), and Stephen J. Harris was supported by the Laboratory Directed Research and Development Program of Lawrence Berkeley National Laboratory under U.S. Department of Energy contract (DE-AC02-05CH11231).

References

1 S. Chen, J. Zhang, L. Nie, X. Hu, Y. Huang, Y. Yu and W. Liu, *Adv. Mater.*, 2021, **33**, 2002325.
2 F. Zhao, S. H. Alahakoon, K. Adair, S. Zhang, W. Xia, W. Li, C. Yu, R. Feng, Y. Hu, J. Liang, X. Lin, Y. Zhao, X. Yang, T.-K. Sham, H. Huang, L. Zhang, S. Zhao, S. Lu, Y. Huang and X. Sun, *Adv. Mater.*, 2021, **33**, 2006577.
3 Y. Zheng, Q. Pan, M. Clites, B. W. Byles, E. Pomerantseva and C. Y. Li, *Adv. Energy Mater.*, 2018, **8**, 1801885.
4 M.-C. Bay, M. Wang, R. Grissa, M. V. F. Heinz, J. Sakamoto and C. Battaglia, *Adv. Energy Mater.*, 2020, **10**, 1902899.
5 X. Feng, H. Fang, N. Wu, P. Liu, P. Jena, J. Nanda and D. Mitlin, *Joule*, 2022, **6**, 543–587.
6 J. Zhu, X. Li, C. Wu, J. Gao, H. Xu, Y. Li, X. Guo, H. Li and W. Zhou, *Angew. Chem., Int. Ed.*, 2021, **60**, 3781–3790.
7 W. Yao, P. Zou, M. Wang, H. Zhan, F. Kang and C. Yang, *Electrochem. Energy Rev.*, 2021, **4**, 601–631.
8 T. Or, S. W. D. Gourley, K. Kaliyappan, Y. Zheng, M. Li and Z. Chen, *Electrochem. Energy Rev.*, 2022, **5**, 20.
9 Y. Ren, Y. Shen, Y. Lin and C.-W. Nan, *Electrochem. Commun.*, 2015, **57**, 27–30.
10 Y. Tang, L. Zhang, J. Chen, H. Sun, T. Yang, Q. Liu, Q. Huang, T. Zhu and J. Huang, *Energy Environ. Sci.*, 2021, **14**, 602–642.
11 J. Janek and W. G. Zeier, *Nat. Energy*, 2016, **1**, 16141.
12 E. J. Cheng, A. Sharafi and J. Sakamoto, *Electrochim. Acta*, 2017, **223**, 85–91.
13 E. Kazyak, R. Garcia-Mendez, W. S. LePage, A. Sharafi, A. L. Davis, A. J. Sanchez, K.-H. Chen, C. Haslam, J. Sakamoto and N. P. Dasgupta, *Matter*, 2020, **2**, 1025–1048.
14 L. Porz, T. Swamy, B. W. Sheldon, D. Rettenwander, T. Frömling, H. L. Thaman, S. Berendts, R. Uecker, W. C. Carter and Y.-M. Chiang, *Adv. Energy Mater.*, 2017, **7**, 1701003.
15 J. Zhao, Y. Tang, Q. Dai, C. Du, Y. Zhang, D. Xue, T. Chen, J. Chen, B. Wang, J. Yao, N. Zhao, Y. Li, S. Xia, X. Guo, S. J. Harris, L. Zhang, S. Zhang, T. Zhu and J. Huang, *Energy Environ. Mater.*, 2022, **5**, 524–532.
16 F. Mo, J. Ruan, S. Sun, Z. Lian, S. Yang, X. Yue, Y. Song, Y.-N. Zhou, F. Fang, G. Sun, S. Peng and D. Sun, *Adv. Energy Mater.*, 2019, **9**, 1902123.
17 Y. Wang, L. Ye, X. Chen and X. Li, *JACS Au*, 2022, **2**, 886–897.
18 L. Ye and X. Li, *Nature*, 2021, **593**, 218–222.
19 Y. He, Y. Zhang, Z. Wang, X. Li, Z. Lü, X. Huang and Z. Liu, *Adv. Funct. Mater.*, 2021, **31**, 2101737.
20 G. J. Rees, D. Spencer Jolly, Z. Ning, T. J. Marrow, G. E. Pavlovskaya and P. G. Bruce, *Angew. Chem., Int. Ed.*, 2021, **60**, 2110–2115.
21 T. Deng, X. Ji, L. Zou, O. Chiekezi, L. Cao, X. Fan, T. R. Adebisi, H.-J. Chang, H. Wang, B. Li, X. Li, C. Wang, D. Reed, J.-G. Zhang, V. L. Sprenkle, C. Wang and X. Lu, *Nat. Nanotechnol.*, 2022, **17**, 269–277.
22 L. Fan and X. Li, *Nano Energy*, 2018, **53**, 630–642.
23 D. Spencer Jolly, Z. Ning, J. E. Darnbrough, J. Kasemchainan, G. O. Hartley, P. Adamson, D. E. J. Armstrong, J. Marrow and P. G. Bruce, *ACS Appl. Mater. Interfaces*, 2020, **12**, 678–685.
24 Y. Chen, Z. Wang, X. Li, X. Yao, C. Wang, Y. Li, W. Xue, D. Yu, S. Y. Kim, F. Yang, A. Kushima, G. Zhang, H. Huang, N. Wu, Y.-W. Mai, J. B. Goodenough and J. Li, *Nature*, 2020, **578**, 251–255.
25 Z. Ning, D. S. Jolly, G. Li, R. De Meyere, S. D. Pu, Y. Chen, J. Kasemchainan, J. Ihli, C. Gong, B. Liu, D. L. R. Melvin, A. Bonnin, O. Magdysyuk, P. Adamson, G. O. Hartley, C. W. Monroe, T. J. Marrow and P. G. Bruce, *Nat. Mater.*, 2021, **20**, 1121–1129.
26 D. C. Hitchcock and L. C. De Jonghe, *J. Am. Ceram. Soc.*, 1983, **66**, c204–c205.
27 R. F. Egerton, *Ultramicroscopy*, 2021, **229**, 113363.
28 K. Ishizuka and N. Uyeda, *Acta Crystallogr., Sect. A: Cryst. Phys., Diffr., Theor. Gen. Crystallogr.*, 1977, **33**, 740–749.